Phenomenological description of bright domain walls in ferroelectric-antiferroelectric layered chalcogenides

Anna N. Morozovska[1,*] Eugene A. Eliseev[2] Kyle Kelley,[3] Yulian M. Vysochanskii[4] Sergei V. Kalinin,[3,†] and Petro Maksymovych[3,‡]

[1]*Institute of Physics, National Academy of Sciences of Ukraine, 46 prospect Nauky, 03028 Kyiv, Ukraine*
[2]*Institute for Problems of Materials Science, National Academy of Sciences of Ukraine, Krjijanovskogo 3, 03142 Kyiv, Ukraine*
[3]*The Center for Nanophase Materials Sciences, Oak Ridge National Laboratory, Oak Ridge, Tennessee 37831, USA*
[4]*Institute of Solid State Physics and Chemistry, Uzhhorod University, 88000 Uzhhorod, Ukraine*

(Received 15 September 2020; accepted 2 November 2020; published 17 November 2020)

Recently, a layered ferroelectric $CuInP_2Se_6$ was shown to exhibit domain walls with locally enhanced piezoresponse—a striking departure from the observations of nominally zero piezoresponse in most ferroelectrics. Although it was proposed that such "bright" domain walls are phase boundaries between ferri- and antiferroelectrically ordered regions of the materials, the physical mechanisms behind the existence and response of these boundaries remain to be understood. Here, using Landau-Ginzburg-Devonshire phenomenology combined with a four sublattices model, we describe quantitatively the bright-contrast and dark-contrast domain boundaries between the antiferroelectric, ferroelectric, or ferrielectric long-range-ordered phases in a layered ferroelectric-antiferroelectric ferroics, such as $CuInP_2(S_{1-y}Se_y)_6$.

DOI: 10.1103/PhysRevB.102.174108

I. INTRODUCTION

Multiferroics—solid-state ferroic materials with coupled and ferromagnetic and antiferromagnetic, ferroelectric and antiferroelectric, or other type long-range ordering [1,2]—have been for many years explored from a fundamental perspective [3–5], including recent studies of unusual polarization switching in thin films [6], domain-wall conduction [7], and atomic scale phenomena at surfaces and interfaces [8–11]. These materials are also beginning to find potential applications for applications, such as the concepts of ferroelectric tunneling barriers, light-assisted ferroic dynamics, spin-driven effects, and ultrafast magnetoelectric switching for memory [12–14].

Recently discovered multiferroics, Cu-based layered chalcogenides, with a chemical formula $CuInP_2Q_6$ (Q is S or Se) [15,16], are promising low-dimensional (e.g., single- or few-layered) uniaxial ferroelectrics [17,18]. S- and Se-based Cu-In compounds have a similar structure of individual layers, with Cu^+ and In^{3+} ions counterdisplaced within individual layers, against the backbone of P_2Q_6 anions [19–21]. Despite the structural similarity, the ferroelectric properties of $CuInP_2S_6$ and $CuInP_2Se_6$ are rather different [19–21]. The spontaneous polarization of the uniaxial ferrielectric $CuInP_2S_6$ ranges from 0.05 to 0.12 C/m^2 [22], and is about 0.025 C/m^2 for the uniaxial ferrielectric $CuInP_2Se_6$ [23]. The values of the ferrielectric phase-transition temperatures are ∼305 K for $CuInP_2S_6$ and ∼230 K for $CuInP_2Se_6$. At that $CuInP_2Se_6$ has an anomalously broad phase transition region [19–21] originating from the coexistence of ferroelectric (FE), or ferrielectric (FEI), and antiferroelectric (AFE) ordering, and an incommensurate phase that precedes ferroelectric ordering [20]. The properties of the intermixed S-Se compound are even more interesting [24–26], possibly involving a Lifshitz transition as well as polar glassy phases and weak dipolar correlations in the lattice [27–29]. These properties seem particularly important for prospective application of these materials as functional components of van der Waals heterostructures [30]. Indeed, recently, Song *et al.* [23] proposed that ultrathin films of $CuInP_2Se_6$ develop an antiferroelectric ground state, with the crossover ferrielectric-antiferroelectric instability occurring at a thickness of ∼6-8 layers. The primary driving force for the crossover is the depolarizing field that favors the antiferroelectric with net zero polarization.

An intriguing recent finding is unusual "bright" domain boundaries in $CuInP_2Se_6$, which have enhanced local piezoelectric response [31] as measured by piezoresponse force microscopy (PFM). The effect was attributed to the coexistence of piezoelectric (FE or FEI) and nonpiezoelectric (AFE) phases in $CuInP_2Se_6$, and the structure of FE-AFE domain boundaries was calculated from density-functional-theory (DFT). However, while the existence of these boundaries was considered plausible based on energy arguments, only qualitative agreement was obtained between observable and simulated properties (compare Figs. 1–3 with Fig. 5 in Ref. [31]). Moreover, the detailed physical mechanism by which these walls become piezoelectrically active, and other relevant properties such as the emergence and mobility of these boundaries, and the applicability of these arguments to other ferroic materials have yet to be understood.

*Corresponding author: anna.n.morozovska@gmail.com
†Corresponding author: sergei2@ornl.gov
‡Corresponding author: maksymovychp@ornl.gov

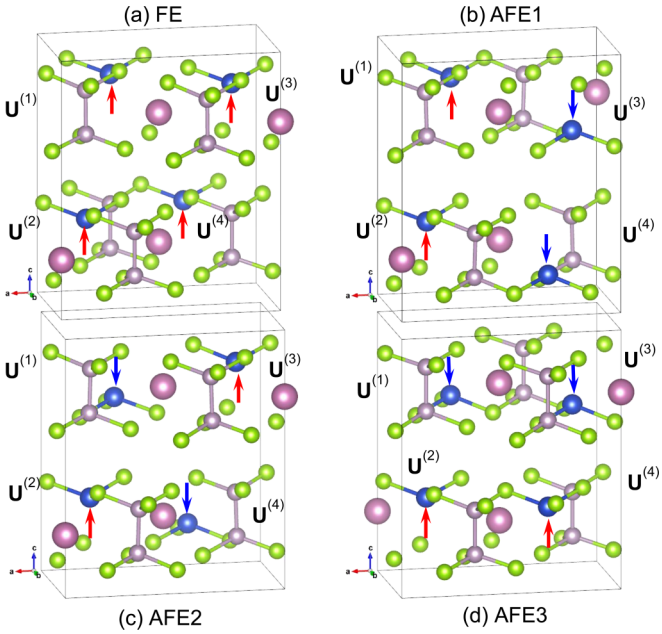

FIG. 1. Atomic structures of $CuInP_2(S_{1-y}Se_y)_6$, obtained by DFT, where the small yellow and blue, small and bigger violet balls are S (or Se) and Cu atoms, P, and In atoms, respectively. The structure is recalculated using DFT data from Ref. [31], which is Open Access under a Creative Commons Attribution 4.0 International License [42]. Here the spatial structure is modified; red and blue arrows inside the atomic groups illustrate the polarization direction for different types of atomic displacements $\boldsymbol{U}^{(m)}$ in the quasihomogeneous ferroelectric (or ferrielectric) FE state (a), and three types of antiferroelectric states: AFE1 (b), AFE2 (c), and AFE3 (d). The orientation of the crystallographic axes a, b, and c is shown at the bottom of each plot.

Here, using Landau-Ginzburg-Devonshire (LGD) approach combined with the recently developed four sublattices model (FSM) [32,33], we explain the emergence and behavior of "bright," "mixed," or "dark" domain walls in a ferrielectric with coexisting AFE and FE long-range ordering. Our theoretical results are in a quantitative agreement with PFM results [31] obtained for Cu-based layered chalcogenide ferrielectric $CuInP_2(S_{1-y}Se_y)_6$, where $0 \leqslant y \leqslant 1$.

II. LGD-FSM APPROACH

LGD-FSM hybrid approach [33] provides a link between "additional order parameters"—atomic displacements **U** of polar-active atomic groups (shown schematically in Fig. 1), and "intrinsic" long-range parameters, such as FE polarization **P** and AFE antipolar parameter **A**. In the framework of FSM Landau expansion of the free energy for a ferrielectric with a nonpolar parent phase contains quadratic and bilinear contributions of the atomic displacements $\mathbf{U}^{(m)}$ [33] and has the form

$$G_{\text{Landau}} = \alpha_{ij}\left(\mathbf{U}^{(\mathrm{i})}, \mathbf{U}^{(\mathrm{j})}\right) + \beta_{ijkl}\left(\mathbf{U}^{(\mathrm{i})}, \mathbf{U}^{(\mathrm{j})}\right)\left(\mathbf{U}^{(\mathrm{k})}, \mathbf{U}^{(\mathrm{l})}\right) + \gamma_{ijklmn}\left(\mathbf{U}^{(\mathrm{i})}, \mathbf{U}^{(\mathrm{j})}\right)\left(\mathbf{U}^{(\mathrm{k})}, \mathbf{U}^{(\mathrm{l})}\right)\left(\mathbf{U}^{(\mathrm{m})}, \mathbf{U}^{(\mathrm{n})}\right). \quad (1)$$

The superscript $m = 1, 2, 3, 4$ enumerates the FSM displacement vectors **U**, which corresponds to one of the four sublattices in the AFE-FE material. The round brackets $(\mathbf{U}^{(\xi)}, \mathbf{U}^{(\zeta)}) = \sum_i U_i^{(\xi)} U_i^{(\zeta)}$ designate the scalar product of the corresponding vectors, where the subscript $i = 1, 2, 3$ enumerates components of the vectors $U_i^{(m)}$ in the m th sublattice. The derivation of Eq. (1) and link between the coefficients α_{ij}, β_{ijkl}, and γ_{ijklmn} with LGD-expansion coefficients can be found in Appendix A of Ref. [33].

Next, using Dzyaloshinsky substitution [34], we relate the electric polarization **P** and three antipolar order parameters (**A**, **B**, and $\tilde{\mathbf{A}}$) with the four atomic displacements $U_i^{(m)}$ of polar-active groups in a ferroic structure as [33]

$$P_i = \frac{q}{2}\left(U_i^{(1)} + U_i^{(2)} + U_i^{(3)} + U_i^{(4)}\right),$$
$$A_i = \frac{q}{2}\left(U_i^{(1)} - U_i^{(2)} - U_i^{(3)} + U_i^{(4)}\right), \quad (2a)$$
$$B_i = \frac{q}{2}\left(U_i^{(1)} - U_i^{(2)} + U_i^{(3)} - U_i^{(4)}\right),$$
$$\tilde{A}_i = \frac{q}{2}\left(U_i^{(1)} + U_i^{(2)} - U_i^{(3)} - U_i^{(4)}\right). \quad (2b)$$

Here $q \cong \frac{Q^*}{V}$ is a dimensionality factor, proportional to the effective Born charge Q^* divided by the unit-cell volume V.

In the most common cases two combinations of atomic displacements out of four can be assumed to be zero, e.g., $\tilde{A}_i = B_i = 0$ (or $A_i = B_i = 0$). Corresponding displacements $U_i^{(m)}$ can be expressed via nonzero polar parameter P_i and antipolar parameter A_i (or $\tilde{A}_i$) as $U_i^{(1)} = U_i^{(4)} = \frac{P_i + A_i}{2q}$ and $U_i^{(2)} = U_i^{(3)} = \frac{P_i - A_i}{2q}$. For any case $U_i^{(1)} = U_i^{(2)} = U_i^{(3)} = U_i^{(4)} = \frac{P_i}{2q}$ in the homogeneous FE phase, while the displacements can be not equal, but of the same sign in a ferrielectric (FI) phase, which can be spatially modulated [32,33]. The displacements $U_i^{(1)} = -U_i^{(2)} = -U_i^{(3)} = U_i^{(4)} = \frac{A_i}{2q}$, or $U_i^{(1)} = U_i^{(2)} = -U_i^{(3)} = -U_i^{(4)} = \frac{\tilde{A}_i}{2q}$, or $U_i^{(1)} = U_i^{(3)} = -U_i^{(2)} = -U_i^{(4)} = \frac{A_i}{2q}$, as well as other combinations of the alternating signs "+" and "−," corresponds to different in AFE1, AFE2, and AFE3 phases, predicted by DFT [31] (see Fig. 1). The case $\tilde{A}_i = B_i = 0$, considered hereinafter, allows us to make elementary algebraic transformation listed in Refs. [32,33], and to reduce Eq. (1) to a conventional Landau formalism, which is used below. The case $A_i = B_i = 0$ can be considered in a very similar way.

A LGD functional of a AFE-FE ferrielectric utilizes Landau-type power expansion, G_{Landau}, that includes the contributions of FE polarization and AFE order components P_i and A_i, as well their gradient energy G_{grad}, elastic and electrostriction coupling energy G_{els}. The functional density G_{LGD} is [33]

$$G_{\text{LGD}} = G_{\text{Landau}} + G_{\text{grad}} + G_{\text{els}}. \quad (3)$$

Electrostatic, elastic, and electrostriction and flexoelectric contributions are neglected in this work, since we considered that uncharged domain walls is a stress-free ferrielectric. The role of electrostriction and flexoelectric coupling was studied earlier [32,33].

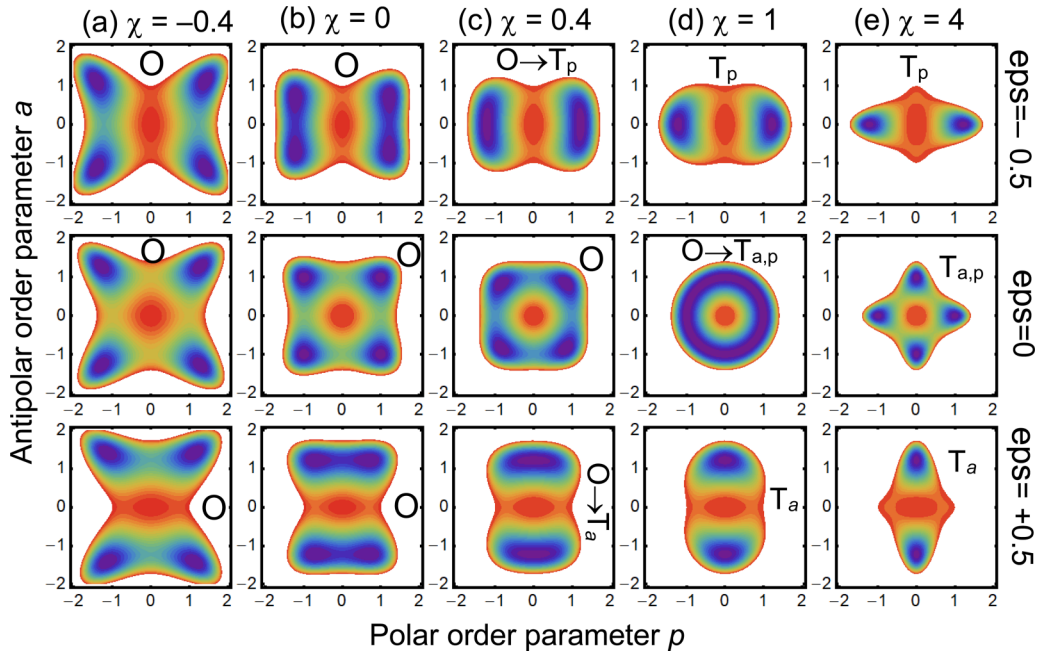

FIG. 2. The free energy (9) as a function of order-parameter components p_1 and p_2 for different values of the AFE-FE coupling constant χ: (a) $\chi = -0.4$, (b) $\chi = 0$, (c) $\chi = 0.4$, (d) $\chi = 1$, and (e) $\chi = 4$. Curie temperatures change parameter $\epsilon = -0.5$ for the top line, $\epsilon = 0$ for the middle line, and $\epsilon = +0.5$ for the bottom line. Red color denotes zero energy, while violet color is its minimal value in relative units. Capital letters O and $T_{a,p}$ denote orthorhombic and tetragonal spatially homogeneous phases, respectively.

The Landau energy G_{Landau} includes FE and AFE energies, and the energy of biquadratic coupling between these order parameters:

$$G_{\text{Landau}} = G_P + G_A + G_{PA}, \tag{4}$$

where the FE and AFE energies are

$$G_P = a_i(T)P_i^2 + a_{ij}P_i^2P_j^2 + a_{ijk}P_i^2P_j^2P_k^2, \tag{5a}$$

$$G_A = c_i(T)A_i^2 + c_{ij}A_i^2A_j^2 + c_{ijk}A_i^2A_j^2A_k^2. \tag{5b}$$

The summation is employed over repeated indexes. The coefficients a_i and c_i are temperature dependent, $a_i = a_T(T - T_C)$, $c_i = c_T(T - T_A)$, where T_C and T_A are the temperatures of FE and AFE phases' absolute instability, respectively. Material parameters of LGD functional corresponding to $CuInP_2S_6$ are relatively well known and can be found, e.g., in Table I in Ref. [35] and references therein. LGD parameters of $CuInP_2Se_6$ are more uncertain (see, e.g., Refs. [24–29]).

Following Kittel-type models, we assume that the temperatures T_C and T_A can be different and coordinate-dependent

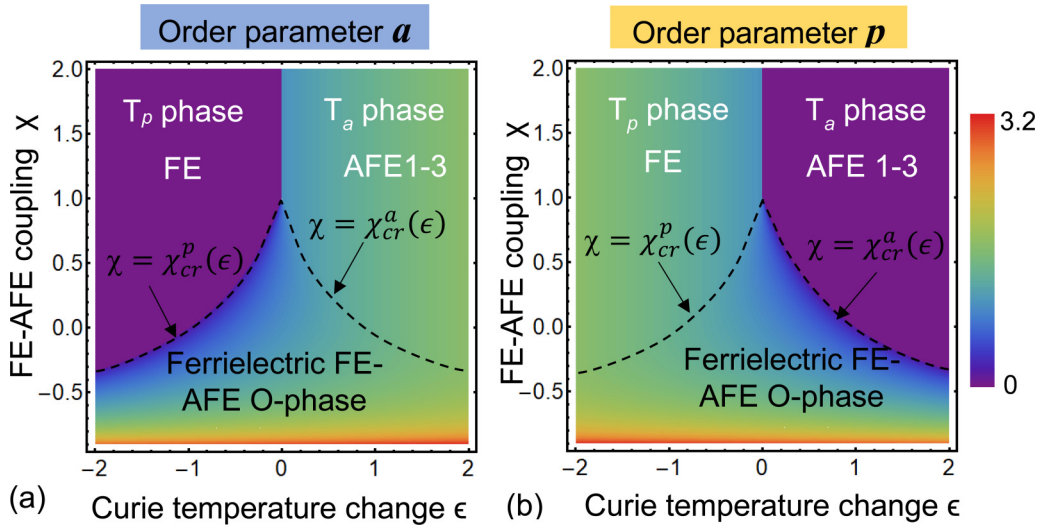

FIG. 3. Color map of order parameters a (a) and p (b) in coordinates χ and ϵ. Color bar on the right represents the color code for the both order parameters.

[33], and that the morphotropic phase boundary (MPB) between FE and AFE phases corresponds to $T_A = T_C = T_0$. Since the energy difference between AFE and FE phases is small in $CuInP_2Se_6$ [31], below we can consider the linear deviations of the FE and AFE temperatures from T_0, $T_C = T_0[1 - \delta\epsilon_C(\boldsymbol{r})]$ and $T_A = T_0[1 + \delta\epsilon_A(\boldsymbol{r})]$, where $|\delta\epsilon_{A,C}(\boldsymbol{r})| \ll 1$. Since the AFE transition takes place in the compound $CuInP_2(S_{1-y}Se_y)_6$ with Se content increase at fixed temperature and all other conditions [24–26], we can assume the equalities of the functions $\delta\epsilon_C = \delta\epsilon_A = \delta\epsilon$; at that the assumption is in complete agreement with Kittel-type models. The assumption allows us to express "Curie-type" temperatures $T_{A,C}$ as **r**-dependent functions in terms of dimensionless parameter ϵ, and correspondingly express the coefficient a_i and c_i through it as follows [33]:

$$a_i = a_0[1 - \epsilon(\boldsymbol{r})], \;\; c_i = a_0[1 + \epsilon(\boldsymbol{r})], \tag{6}$$

where $a_0 = a_T(T_0 - T)$ and $\epsilon(\boldsymbol{r}) = \frac{T_0}{T_0 - T}\delta\epsilon(\boldsymbol{r})$. Since the AFE transition takes place in $CuInP_2(S_{1-y}Se_y)_6$ with "y" increase at the fixed other conditions, we can regard the higher coefficients in Eqs. (5a) and (5b) are ϵ-independent and equal, i.e., $a_{ij} = c_{ij}$ and $a_{ijk} = c_{ijk}$. Since $a_0 < 0$ at $T_0 < T$, the condition $\epsilon(\boldsymbol{r}) < 0$ supports the stability of the FE phase, and the condition $\epsilon(\boldsymbol{r}) > 0$ supports the AFE phase stability. The MPB between FE and AFE phases corresponds to $\epsilon = 0$.

Note that the parameter $\epsilon(\boldsymbol{r})$ plays a central role in all further theoretical analysis, and basically it is a way to control the temperatures of FE and AFE phases' absolute instability, and "biasing" the system toward the desired state. In a definite sense the parameter $\epsilon(\boldsymbol{r})$ can be associated with the spatial changes of T_A and T_C, being a close analog to a "random temperature" model for the Curie temperature variation in disordered (e.g., relaxor) ferroelectrics. It is worth noting that the off-stoichiometry $\delta y(\boldsymbol{r})$ of y content in $CuInP_2(S_{1-y}Se_y)_6$ [24–29] can be a way to realize the parameter $\epsilon(\boldsymbol{r})$ in practice. Another way may be a surface chemistry.

Biquadratic coupling energy between FE and AFE orders has the form [33]

$$G_{PA} = t_{ijkl}P_iP_jA_kA_l. \tag{7}$$

In Eq. (7) we included only the biquadratic coupling between FE and AFE orders, whose strength is proportional to the tensor t_{ijkl}, assuming that the lower-order coupling of P_i, A_i, and their gradients is absent due to the symmetry of the nonpolar parent phase.

The gradient (G_{grad}) energy is

$$G_{\text{grad}} = g_{ijkl}\left(\frac{\partial P_i}{\partial x_k}\frac{\partial P_j}{\partial x_l} + \frac{\partial A_i}{\partial x_k}\frac{\partial A_j}{\partial x_l}\right), \tag{8}$$

where g_{ijkl} is the gradient tensor, which is the same for FE and AFE long-range order parameters due to the sublattice symmetry.

All calculations below use a continuum media LGD-FSM approach (1)–(8), whose applicability has several limitations. The main criteria for the quantitative validity of the LGD-FSM approach are the scales of continuous calculations, which are equal to the correlation lengths of the polar and antipolar order parameters, which are equal to $L_{pi} = \sqrt{|g_{44}/(2a_i)|}$ and $L_{ai} = \sqrt{|g_{44}/(2c_i)|}$ for the second-order phase transitions. These lengths must be more that several lattice constants for semiquantitative validity of the LGD-FSM approach [36]. When they well exceed ten lattice constants numerical results become quantitatively valid. Since L_{pi} and L_{ai} are minimal at $T = 0$ K and diverge at $T \to T_0$, their minimal values $\sim \sqrt{g_{44}/a_T T_0}$ define the ranges of LGD approach validity far from T_0. The values $a_T T_0$ are tabulated for most inorganic ferroics, but the values of the gradient coefficient g_{44} demonstrate a wide discrepancy (up to several orders of magnitude) from different experiments, such as HR STEM and PFM measurements of the uncharged domain-wall width in ferroelectrics and ferrielectrics grown in the form of single crystals, or thin films. Moreover, the values of g_{ijkl} calculated from the density functional theory (DFT) can strongly vary in sign and magnitude. Hence the discrepancy of L_{pi} and L_{ai} are rather strong, and should be compared with a lattice constant for any concrete case. Another limitation is the inclusion of random electric fields created by defects, which is hardly possible within the proposed type of LGD-FSM approach, where only the "random" temperature-type defects can be included via the random variation of $\epsilon(\boldsymbol{r})$. Complementary to the LGD-FSM approach, the random crystal fields can be considered in the frame of the Blume-Capel (BC) model, which is a simplification of Blume-Emery-Griffiths (BEG) model (see, e.g., Ref. [37]). However, the consideration of BEG and BC models is not in the scope of this work.

III. FREE-ENERGY LANDSCAPE AND PHASE DIAGRAMS OF THE ORDER PARAMETERS

For a uniaxial FE-AFE ferroelectric with a second-order phase transition, the bulk density of LGD free energy (3) can be written in dimensionless variables as

$$g_{\text{LGD}} = -(1-\epsilon)\frac{p^2}{2} - (1+\epsilon)\frac{a^2}{2} + \frac{p^4 + a^4}{4} + \frac{\chi}{2}p^2a^2 + \frac{g}{2}\left[\left(\frac{dp}{dx}\right)^2 + \left(\frac{da}{dx}\right)^2\right], \tag{9}$$

where the dimensionless order parameters $p = P/P_S$ and $a = A/P_S$ are introduced; P_S is a spontaneous polarization in the FE phase, and g is the component of the polarization gradient tensor g_{ijkl}. In Eq. (9) we omitted all six-order terms for a considered case of the second-order phase transitions. Following Ref. [33], we regard that the strength of the FE-AFE coupling term, $\frac{\chi}{2}p^2a^2$, is defined by dimensionless temperature-independent constant χ, that is related with the corresponding component of the tensor t_{ijkl} in Eq. (7) as $t_{ijkl} = \chi t^0_{ijkl}$. Since the FE-AFE coupling should depend on Se content y, the parameter χ is y dependent.

For zero gradients, minimization of the free energy (9) allows one orthorhombic (**O**) and two tetragonal ($\mathbf{T}_a$ and $\mathbf{T}_p$) phases. The spontaneous values of the order parameter, corresponding free energy, existence, and stability conditions of these phases are summarized in Table I, where the critical values of the FE-AFE coupling constant χ,

TABLE I. Thermodynamic phases, order parameters, and phase boundaries.

Phase	Order parameters	Free energy	Existence	Absolute stability	Phase boundaries[a]
T_p	$p=\pm\sqrt{1-\epsilon}$ $a=0$	$-\frac{1}{4}(1-\epsilon)^2$	$\chi > \chi_{cr}^{p}(\epsilon)$ and $\epsilon < 1$	$\chi > \chi_{cr}^{p}(\epsilon)$ and $\epsilon < 0$	T_p with T_a $\epsilon = 0$ at $\chi > 1$
T_a	$p=0$ $a=\pm\sqrt{1+\epsilon}$	$-\frac{1}{4}(1+\epsilon)^2$	$\chi > \chi_{cr}^{a}(\epsilon)$ and $\epsilon > -1$	$\chi > \chi_{cr}^{a}(\epsilon)$ and $\epsilon > 0$	T_p with O $\chi = \chi_{cr}^{p}(\epsilon)$ at $\chi^2 < 1$
O	$p=\pm\sqrt{\frac{1-\epsilon-\chi(1+\epsilon)}{1-\chi^2}}$ $a=\pm\sqrt{\frac{1+\epsilon-\chi(1-\epsilon)}{1-\chi^2}}$	$-\frac{1+\epsilon^2-\chi(1-\epsilon^2)}{2(1-\chi^2)}$	$-\frac{1-\chi}{1+\chi} < \epsilon < \frac{1-\chi}{1+\chi}$ and $\chi^2 < 1$	$-\frac{1-\chi}{1+\chi} < \epsilon < \frac{1-\chi}{1+\chi}$ and $\chi^2 < 1$	T_a with O $\chi = \chi_{cr}^{a}(\epsilon)$ at $\chi^2 < 1$

[a]In a particular case $\chi = 1$ and $\epsilon = 0$, the "round" potential well with the equilibrium values of the order parameters, given by equation $p^2 + a^2 = 1$, is realized, so that phases "O", "T_a" and "T_b" become undistiguishable.

corresponding to FE-mixed phase and AFE-mixed phase boundaries, are $\chi_{cr}^{p}(\epsilon) = \frac{1+\epsilon}{1-\epsilon}$ and $\chi_{cr}^{a}(\epsilon) = \frac{1-\epsilon}{1+\epsilon}$ (see Appendix A in the Supplemental Material [38]).

The free energy (9) as a function of polar and antipolar order parameters, p and a, is shown in Fig. 2 for different ϵ and χ values, and zero gradient coefficient $g = 0$. From the figure one can see that, in dependence on the values of parameters ϵ and χ, the free energy can contain four potential wells, separated by four saddles and central maximum (e.g., for $\chi < 0$, or for $\epsilon = 0$ and $\chi \neq 1$), or two potential wells, separated by two saddles and central maximum (e.g., for $\chi > 1$ and $\epsilon \neq 0$), or a round well (indicating a $O \rightarrow T_{a,p}$ transition) is realized in a particular case $\chi = 1$ and $\epsilon = 0$. However, even in the case of four wells, corresponding to both nonzero order parameters, $p = \pm\sqrt{\frac{1-\epsilon-\chi(1+\epsilon)}{1-\chi^2}}$ and $a = \pm\sqrt{\frac{1+\epsilon-\chi(1-\epsilon)}{1-\chi^2}}$, only p values can be observable experimentally. Generally speaking, an LGD-type phenomenological model can describe the shape of the multiwell potential, but the microscopic origin of the order parameter(s), which form this potential, is not explained by the model. As a rule, the microscopic origin can be explained by *ab initio* theory (see, e.g., [22]), which allows us to relate LGD order parameters, p and a, with a FSM model.

The dependencies (color map) of the order parameters a and p on the dimensionless transition temperatures change ϵ and FE-AFE coupling constant χ are shown in Figs. 3(a) and 3(b), respectively. The color maps of a and p are superimposed on the phase diagrams containing the regions of the FE, AFE, and ferrielectric AFE-FE phases. The region of the phase stability depends on the parameters ϵ and χ. The quasihomogeneous FE T_p phase, with $p \neq 0$ and $a = 0$, is stable at $\epsilon < 0$, and the quasihomogeneous AFE1-3 T_a phases, with $a \neq 0$ and $p = 0$, are stable at $\epsilon > 0$. The FE-AFE coexistence boundary $\epsilon = 0$ is a straight vertical line, independent on χ and existing for $\chi > 1$. Both order parameters are nonzero in a mixed AFE-FE O-phase. At that, the boundary between the FE and AFE phases is $\epsilon = 0$; the boundary between FE and mixed FE-AFE phases is described by the equation $\chi(\epsilon) = \chi_{cr}^{p}(\epsilon) = \frac{1+\epsilon}{1-\epsilon}$, and the boundary between the AFE and mixed FE-AFE phases is described by the equation $\chi(\epsilon) = \chi_{cr}^{a}(\epsilon) = \frac{1-\epsilon}{1+\epsilon}$. The color maps shown in Figs. 3(a) and 3(b) are in agreement with the phase diagram shown in Fig. 2(b) from Ref. [33].

IV. BRIGHT AND DARK DOMAIN WALLS

To study the coexistence of FE and AFE phases and therefore the properties of domain-wall boundaries, while allowing for the gradient effects in a uniaxial ferroelectric, one should solve the coupled Euler-Lagrange equations obtained by the variation of the energy (9):

$$-[1-\epsilon(\boldsymbol{x})]p + p^3 + \chi p a^2 - g\Delta p = 0, \tag{10a}$$

$$-[1+\epsilon(\boldsymbol{x})]a + a^3 + \chi p^2 a - g\Delta a = 0. \tag{10b}$$

Here the dimensionless order parameters $p = P/P_S$ and $a = A/P_S$ are introduced, where P_S is a spontaneous polarization in the FE phase, and $\Delta = \frac{d^2}{dx_1^2} + \frac{d^2}{dx_2^2} + \frac{d^2}{dx_3^2}$ is a Laplacian. To avoid the emergence of a depolarization field, the direction $\mathbf{x}$ should be perpendicular to $\boldsymbol{P}$ vector. In the absence of a depolarizing field, electrostatic effects do not play an important role in further discussion, while in reality these effects are the main driving force for the emergence of the domain structure.

Equations (10) should be supplemented by specific boundary conditions, e.g., the order parameter periodicity (or antiperiodicity) in a ferrielectric infinite in the x direction, e.g., $p(-L) = \pm p(L)$, $a(-L) = \pm a(L)$, where L is the size of the computation region. The initial conditions can contain different numbers of uncharged p and a domain walls, or small random distributions of the order parameters. Note that the so-called "natural" boundary conditions, $\frac{\partial}{\partial x}p(\pm L) = \frac{\partial}{\partial x}a(\pm L) = 0$, typically lead to the system relaxation to the homogeneous state, especially in the case of initial random distributions.

Distributions of the dimensionless FE and AFE order parameters p (blue curves) and a (red curves) calculated by finite element modeling (FEM) for coordinate-independent and coordinate-independent parameter $\epsilon(x)$ are shown in Figs. 4(a)–4(d), respectively. FEM was performed in COMSOL@Multiphysics.

The profiles of the order parameters across the uncharged domain boundary in the FE phase of the bulk material, corresponding to the negative constant $\epsilon(\boldsymbol{x}) = \epsilon_0$, are shown in Fig. 4(a). Here one can see an Ising-type 180° FE p wall (blue tanh-like profile) with a noticeable maximum of AFE order parameter a at the FE wall (red humplike profile). For the situation shown in Fig. 4(a) the antiperiodic boundary conditions were applied for the order parameter p, $p(-L) = -p(L)$, and the initial distribution of $p(x)$ was a single domain

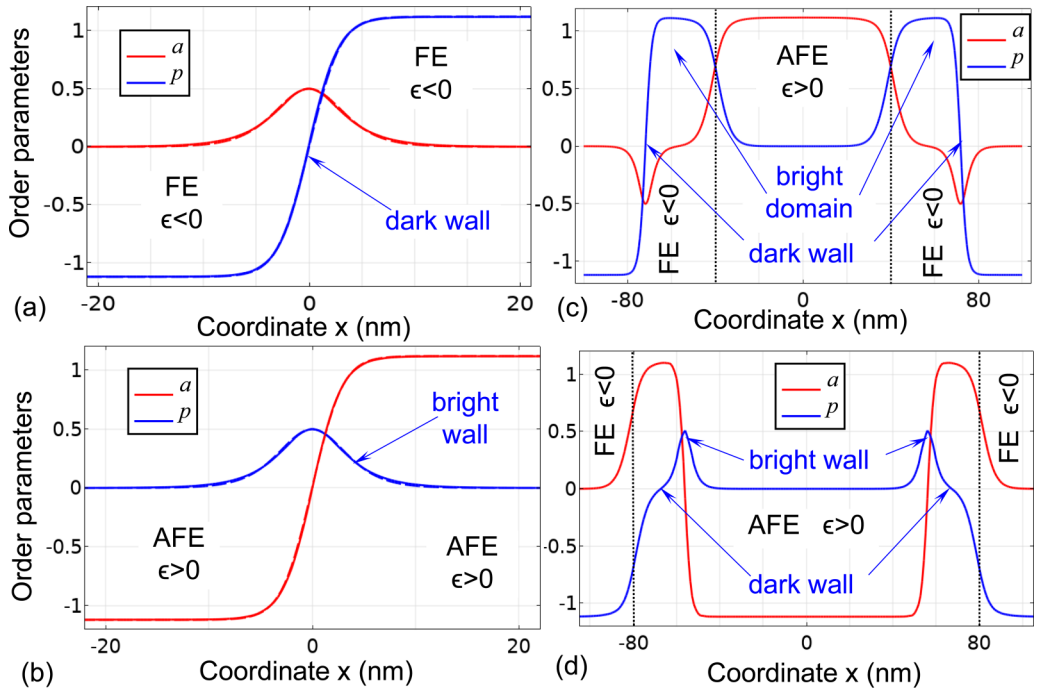

FIG. 4. Distributions of the FE and AFE order parameters, p (blue curves) and a (red curves), respectively. Plots (a) and (b) illustrate the profiles of a and p at the domain wall in FE and AFE phases, corresponding to $\epsilon_0 = -\frac{1}{4}$ and $\epsilon_0 = +\frac{1}{4}$, respectively. Plots (c) and (d) show the profiles of a and p at the boundaries between FE and AFE phases, induced by the function $\epsilon(x) = \epsilon_0[\tanh(\frac{x+x_0}{L_d}) - 1 - \tanh(\frac{x-x_0}{L_d})]$. The difference between (c) and (d) is in the initial distribution of the order parameters and AFE region width. Other parameters: $\epsilon_0 = 0.25$, $L_d = 10$ nm, $x_0 = 40$ nm (c) or 80 nm (d), $\chi = 1$, $g = 4\,\text{nm}^2$. Solid curves in all plots are calculated by FEM. Dashed curves in plots (a) and (d) are calculated from Eqs. (11a) and (11b) with fitting parameters listed in the text. Dotted vertical lines in plots (c) and (d) denote the points where $\epsilon \approx 0$.

wall. The solution becomes insensitive to the boundary conditions for $a(\pm L)$ when $L \gg 10$ nm, but the best convergence corresponds to the periodic condition, $a(-L) = a(L)$. The initial distribution of $a(x)$ was either zero or a small random function.

The profiles of the order parameters across the domain boundary in the AFE phase, corresponding to the positive constant $\epsilon(x) = \epsilon_0$, is shown in Fig. 4(b). The picture is opposite to Fig. 4(a), and here one can see an Ising-type 180° AFE a wall (red tanh-like profile) with a p maximum at the wall (blue humplike profile). Hence, the is a bright domain wall located in the AFE phase region. We regard that the wall "brightness" is associated with polarization maximum at the domain wall. For the situation shown in Fig. 4(b) the antiperiodic boundary conditions were applied for the a, $a(-L) = -a(L)$, and the initial distribution of $a(x)$ was a single domain wall. For p we used the periodic boundary conditions, $p(-L) = \pm p(L)$, and the initial distribution of $p(x)$ was either zero or small random function.

Next, let us assume that the profile $\epsilon(\boldsymbol{x})$ has a form of a stripe of finite thickness $2x_0$, and use the "smooth" function to describe the profile, $\epsilon(x) = \epsilon_0[\tanh(\frac{x+x_0}{L_d}) - 1 - \tanh(\frac{x-x_0}{L_d})]$, with parameters $\epsilon_0 = 0.25$, $L_d = 10$ nm, and $x_0 = 40$ nm [Fig. 4(c)] or 80 nm [Fig. 4(d)]. Typical profiles of the FE and AFE order parameters, shown in Figs. 4(c) and 4(d), are calculated for periodic boundary conditions, $p(-L) = p(L)$ and $a(-L) = a(L)$, and different initial distributions of p and a corresponding to different numbers of a walls in the AFE layer and p walls in the FE layers near the inclusion of the AFE layer, respectively. All of these domain walls exhibit a complex structure: vanishing of one of the order parameters is accompanied by a maximum of the other one. In these cases, shown Figs. 4(c) and 4(d), there are either two bright domains located right outside the FE-AFE boundary, or two bright domain walls located inside the AFE region near the AFE-FE boundary.

When a PFM scans the material in a FE phase, an image of an 180° domain wall is the region of gradually reduced contrast due to the decreasing FE order up to zero polarization in the center of the domain wall [31]. The structural AFE order parameter (e.g., the predicted maximum at the wall) cannot be directly observed by PFM. Thus, for a material in the AFE phase, the PFM imaging of the AFE domain walls looks opposite to the walls in the FE phase. Bulk AFE domains do not give any PFM response; the contrast appears only near the AFE antiphase domain walls with local polarization. A maximally localized PFM response will be observed here. Therefore, we can conclude that dark domain walls are observed by PFM in the FE phase, and bright PFM domain walls should be observed in the AFE phase, or at the AFE-FE boundaries. The conclusion is in a qualitative agreement with recent PFM experiments [31].

However, one of the features we should emphasize is that the domain walls in our model acts as "pair entities" caused by the symmetry of periodic boundary conditions. There is always a bright-dark pair [see Figs. 4(c) and 4(d)]. In pure phases, pure FE or pure AFE, the pair is colocated, and so we see a FE or AFE wall, respectively [see Figs. 4(a) and 4(b)].

The pair splits in space near symmetric AFE-FE boundaries separating AFE region from FE regions, but it is still stable. The question about the pair experimental observation is discussed in the next section.

To analyze FEM results, shown in Figs. 4, we used the approximate analytical expressions for the order-parameter profiles, which can be found for several specific cases, namely for $\chi \approx 0$ and arbitrary $|\epsilon(\boldsymbol{x})| < 1$, or for $\chi \approx 6[1 \pm \epsilon(\boldsymbol{x})]$ and very small $|\epsilon(\boldsymbol{x})| \ll 1$. In the first case the solution is a single tanh profile [39], and a superposition of several tanh profiles [40,41] in the second case. While the tanh profiles are not general, FEM confirms that slightly more complex trial functions can be used to describe the dark (DW) and bright (BW) p walls in FE and AFE phases, namely

$$\text{DW:}\quad p(x) = \frac{p_s}{2}\left[\tanh\left(\frac{x+x_w}{L_p}\right) + \tanh\left(\frac{x-x_w}{L_p}\right)\right],$$
$$a(x) = \frac{a_s}{2}\left[\tanh\left(\frac{x+x_w}{L_a}\right) - \tanh\left(\frac{x-x_w}{L_a}\right)\right], \quad (11a)$$
$$\text{BW:}\quad p(x) = \frac{p_s}{2}\left[\tanh\left(\frac{x+x_w}{L_p}\right) - \tanh\left(\frac{x-x_w}{L_p}\right)\right],$$
$$a(x) = \frac{a_s}{2}\left[\tanh\left(\frac{x+x_w}{L_a}\right) + \tanh\left(\frac{x-x_w}{L_a}\right)\right]. \quad (11b)$$

Here the amplitudes p_s and a_s define FE and AFE order parameters far from the wall, because $p(x \to \pm\infty) \to \pm p_s$ for dark walls and $a(x \to \pm\infty) \to a_s$ for bright ones. The correlation lengths L_p and L_a and the shift x_w define the width of the $p(x)$ and $a(x)$ domain walls, respectively. Also $|x| - x_w$ is the distance from center of the FE-AFE boundary $x = 0$. The height of the p maximum located at the bright p wall is equal to $p_s \tanh(\frac{x_w}{L_p})$ and its width is an order of $2L_p$. Quite symmetrically, the height of the a maximum located at the dark p wall is equal to $a_s \tanh(\frac{x_w}{L_a})$ and its width is an order of $2L_a$.

As an example, dashed curves in Fig. 4(a), which are calculated from analytical expressions (11a) with parameters $p_s = 1.12$, $a_s = 2.16$, $L_p = 2.6$ nm, $L_a = 4.25$ nm, and $x_w = 1$ nm, fit with very high accuracy (point-to-point) solid curves calculated by FEM. The dashed curves in Fig. 4(b) are calculated from expressions (11b) with parameters $a_s = 1.12$, $p_s = 2.16$, $L_a = 2.6$ nm, $L_p = 4.25$ nm, and $x_w = 1$ nm, which are related with the parameters of the dashed curves in Fig. 4(a) by expected substitution $p \leftrightarrow a$.

In general, five values p_s, a_s, L_p, L_a, and x_w are variational parameters, which can be determined after substitution of Eqs. (11) in the free energy (3) and further integration and minimization over these parameters. It appeared that the proportionalities for amplitudes $p_s \sim \sqrt{1-\epsilon}$ and $a_s \sim \sqrt{1+\epsilon}$, and for correlation lengths $L_p \sim \sqrt{\frac{2g}{1-\epsilon}}$ and $L_a \sim \sqrt{\frac{2g}{1+\epsilon}}$ are approximately valid.

The changes of local strains induced by the variation of ϵ can be estimated from the expression

$$\delta u_{in} = V_{in}\epsilon(y,\boldsymbol{x}) + d_{ink}P_k + Q^P_{inkj}(P_kP_j - P_{Sk}P_{Sj}) + Q^A_{inkj}(A_kA_j - A_{Sk}A_{Sj}), \quad (12)$$

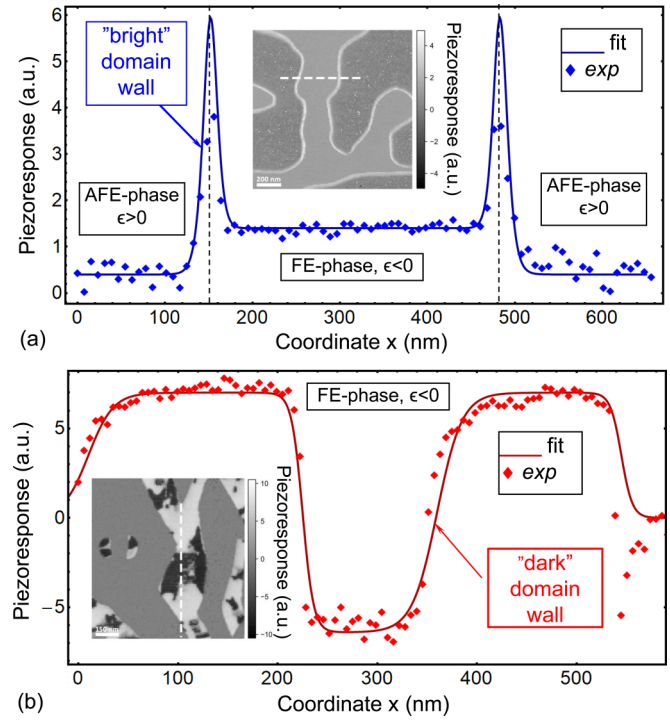

FIG. 5. Local piezoresponse (in arbitrary units) at $CuInP_2Se_6$ (a) and $Cu_{1-x}InP_2S_6$ (b) surfaces. Red and blue diamonds are PFM data [31] measured at 140 K in ultrahigh vacuum for $CuInP_2Se_6$ and that of $CuInP_2S_6$ at room temperature in controlled environment. Solid dark red and blue curves are fitted by Eq. (13a) with parameters provided in the text. Black arrows point to the regions of the bright (a) and dark (b) domain walls. Line profiles of piezoresponses (a),(b) were measured along the white dashed lines, crossing domain boundaries in inset to plots (a) and (b), respectively. Color insets are adapted from [31] using Open Access under a Creative Commons Attribution 4.0 International License [43].

where V_{in} is a Vegard stress tensor, d_{ink} is a piezoelectric tensor, Q^P_{inkj} and Q^A_{inkj} are electrostriction tensors for FE and AFE order parameters, respectively.

In accordance with our model, which predicts the emergence of dark or bright domain walls at the boundary between FE and AFE phases, the spatial gradients of the FE and AFE transition temperatures, $\frac{d\epsilon}{dx}$, can lead to the suppressed or enhanced local electromechanical response at the boundaries between the FE, FEI, and AFE phases. Moreover, mixed FE-AFE phases can be spatially modulated and at the same time incommensurate.

V. COMPARISON WITH EXPERIMENT

Using low-temperature PFM, the coexistence of piezoelectric and nonpiezoelectric phases separated by unusual bright domain walls with enhanced piezoelectric response has been revealed in $CuInP_2Se_6$ [31], and explained by enhanced piezoresponse at the FE(FEI)-AFE phase boundary [see Fig. 5(a)]. The AFE state was partially polarized, with inclusions of structurally different FEI domains enclosed by the "enhanced" phase boundaries, which indicates the coexistence of AFE, FEI, and FE-AFE phases, and the conclusion was supported by optical spectroscopies and DFT calculations

as detailed in Ref. [31]. The layered ferroelectric $CuInP_2S_6$ only revealed a dark domain by comparison [see Fig. 5(b)].

The bright and dark domain walls are shown in Figs. 5(a) and 5(b), respectively, and are in qualitative agreement with our theoretical results shown in Fig. 4. Blue and red curves in Figs. 5(a) and 5(b) demonstrate the quantitative agreement between experimental data points [31] and theoretical model evolved here.

However, it is important that we see a bright wall in Fig. 5(a), whereas according to Figs. 4(c) and 4(d), it should be a bright-dark pair. We can argue that the dark FE wall can be anywhere in the signal, and so its detection requires careful adjustment of experimental offsets. A follow-on point to this is which of Fig. 4(c) or Fig. 4(d) is better consistent with experiment—a bright domain or a bright domain wall? The width of bright regions extracted from experimental data can help to answer. So, for detailed experimental matching, the analysis of the PFM signal as a function of applied electric field (to rule out electrostatic effects) is highly recommended. Another experimental idea would be to try to switch FE and AFE domains separately from their domain boundaries. Observation of bright and dark domain walls independently from the properties of the AFE/FE boundary would serve well to understand the imaging and piezoelectric property of the boundary itself.

To fit the PFM response (PR) of $CuInP_2Se_6$, we use the kink-type profiles similar to Eqs. (11), which are inherent to the diffuse Bloch-Ising-type domain walls and typical for multiaxial ferroelectrics in mixed phases [39,41]. The functions are

$$\mathrm{PR}(x) = u_0 + \sum_{i=1}^{4} u_i \tanh\left(\frac{x - x_i}{w_i}\right). \tag{13a}$$

The number "4" in the sum originates from two bright well-separated domain walls, each of which is described by two tanh functions with their own amplitudes u_i, intrinsic width w_i, and shifts x_i. The constant offset level is U_0. The best fitting to the blue symbols [31] corresponds to the following parameters: $u_0 = 0.4$, $u_1 = -u_4 = 11$, $u_2 = -u_3 = -10.5$ (a.u.), $w_1 = w_4 = 11$, $w_2 = w_3 = 10$ (nm), and $x_1 = 150$, $x_2 = 155$, $x_3 = 480$, $x_4 = 485$ (nm). Using the symmetry of the fitting parameters the solution can be rewritten as

$$\mathrm{PR}(x) = u_0 + u_1\left[\tanh\left(\frac{x - x_1}{w_1}\right) - \tanh\left(\frac{x - x_4}{w_1}\right)\right] + u_2\left[\tanh\left(\frac{x - x_2}{w_2}\right) - \tanh\left(\frac{x - x_3}{w_2}\right)\right]. \tag{13b}$$

Actually, it was shown [41], that the difference (or sum) of two tanh functions with the same scale parameter w can be considered as trial functions describing Bloch-Ising-type domain walls.

To fit the PFM response of $CuInP_2S_6$ in the ferroelectric phase, at first we used the Jacobi elliptic functions—"snoids," each of which are exact solutions for uncharged domain walls satisfying the static LGD equations with cubic nonlinearity and without depolarization fields [41]:

$$\mathrm{PR}(x) = u_0 + \sum_{i=1}^{2} u_i(x)\mathrm{sn}\left(\frac{x - x_i}{w_i\sqrt{1+m}}\middle| m\right). \tag{13c}$$

where the constant offset u_0, slow-varying (due to the presence of surface defects) amplitudes $u_i(x)$, "module" $0 \leqslant m \leqslant 1$, and "shifts" x_i of snoids are fitting parameters. The best fitting was to the red symbols [31] obtained using Eqs. (13c) corresponding to $m = 0.999$, i.e., it tends unity. This result means that the wall profile is strongly nonlinear, and the limit $\mathrm{sn}(\frac{x-x_i}{w_i\sqrt{1+m}}|m)|_{m\to 1} \to \tanh(\frac{x-x_i}{2w_i})$ is well grounded. That is why, as a next stage, we used the functional form (13a) for the fitting of local PR and determine that the following best fitting parameters: $u_0 = 0$, $u_1 = -u_4 = 3.5$, $u_2 = -u_3 = -6.7$ (a.u.), $w_1 = w_3 = 25$, $w_2 = w_4 = 11$ (nm), and $x_1 = 10$, $x_2 = 225$, $x_3 = 360$, $x_4 = 545$ (nm), correspond to $CuInP_2S_6$.

Since in both cases Eq. (13b) appeared to be an optimal fitting, we can comment on the fitting parameters and try to extract some information about the internal parameters $\epsilon(\boldsymbol{x})$, χ, g, and x_{wi} in Eqs. (11) from them. The main differences appear to be three times larger, $u_1 = -u_4 = 11$ for $CuInP_2Se_6$, in comparison to $u_1 = -u_4 = 3.5$ for $CuInP_2S_6$; at that $u_2 = -u_3 = -10.5$ for $CuInP_2Se_6$ are relatively close to $u_2 = -u_3 = -6.7$ for $CuInP_2S_6$. We note the twice difference in the widths $w_1 = w_3 = 25$ nm and $w_2 = w_4 = 11$ nm for the $CuInP_2Se_6$, in contrast to almost the same widths $w_1 = w_4 = 11$ nm $\sim$ $w_2 = w_3 = 10$ nm for $CuInP_2S_6$. Compare the big difference in shifts $x_1 - x_2 = -215$ nm, $x_3 - x_4 = -185$ nm for $CuInP_2S_6$ with small and the same difference $x_1 - x_2 = x_3 - x_4 = -5$ nm for $CuInP_2Se_6$. Exactly the difference determines the crossover from the "humps" at bright walls to zero values at dark walls. Note that the alternating signs of u_i are all the same for both sulfide and selenide compounds. These trends are in a qualitative agreement with the tanh-like fitting by Eqs. (11) of the FEM solution of Eqs. (10). Actually for $\epsilon > 0$, p_s is smaller than a_s, and L_p is higher than L_a. The situation is opposite for $\epsilon < 0$, when $p_s > a_s$ and $L_p < L_a$.

Based on the domain-wall widths, extracted from Fig. 5(a), FEM results are shown in Fig. 4(d). Intuitively the result is clear, because Fig. 4(c) contains wider regions of brightness, and the existence of bright domains in a ferrielectric $CuInP_2Se_6$ is something "mixed" between FE and AFE states. Note that the consideration of domain boundaries originated from the mid van der Walls FE or mid van der Walls AFE states such as those found in $CuInP_2S_6$ [22] is outside the scope of our model.

VI. CONCLUSION

The main result of this work is the explanation of the unusual domain-wall structure in FE, AFE, and mixed AFE-FE phases of Cu-based layered ferrielectric $CuInP_2(S_{1-y}Se_y)_6$. In accordance with the LGD-FSM approach, proposed by us earlier [32,33], the spatial gradient of the local Curie temperature can lead to the coexistence of the FE, AFE, and spatially modulated ferrielectric FE-AFE phases, as well as to the suppressed or enhanced local electromechanical contrast at the boundaries between the phases. Note that the aforementioned behaviors originated from the system tendency to minimize LGD-FSM free energy under certain conditions imposed on the control parameters (Curie temperatures variation ϵ and the coupling strength χ between FE and AFE orders).

Since dark or bright boundaries have been recently observed by PFM and optical spectroscopy experiments for $CuInP_2(S_{1-y}Se_y)_6$ (where $y = 0$ and $y = 1$), our theoretical results, being in quantitative agreement with the experiments [31], provide insight to the origin of unusual domain boundaries in FE-AFE layered ferrielectrics.

ACKNOWLEDGMENTS

Authors gratefully acknowledge Dr. J. A. Brehm for useful discussions. Authors acknowledge L. Tao, A. O'Hara, and S. Pantelides for sharing calculated structures of antiferroelectric $CuInP_2Se_6$. This material is based upon work (S.V.K., P.M.) supported by the Division of Materials Science and Engineering, Office of Science, Office of Basic Energy Sciences, U.S. Department of Energy, and performed in the Center for Nanophase Materials Sciences, supported by the Division of Scientific User Facilities. A portion of FEM performed in the Center for Nanophase Materials Sciences, which is a DOE Office of Science User Facility (CNMS). A.N.M. was supported by the National Research Foundation of Ukraine (Grant Application No. 2020.02/0027 and Contract N 52/02.2020).

A.N.M., P.M., and S.V.K. generated the research idea and proposed the theoretical model. A.N.M. derived analytical results, interpreted numerical results, obtained by E.A.E, compared with experiment, performed by K.K. and P.M., and wrote the manuscript draft. S.V.K., Y.M.V., and P.M. worked on the results discussion and manuscript improvement.

[1] M. Fiebig, Revival of the magnetoelectric effect, J. Phys. D: Appl. Phys. **38**, R123 (2005).

[2] N. A. Spaldin and M. Fiebig, The renaissance of magnetoelectric multiferroics, Science **309**, 391 (2005).

[3] A. P. Pyatakov and A. K. Zvezdin, Magnetoelectric and multiferroic media, Phys. Usp. **55**, 557 (2012).

[4] M. Fiebig, T. Lottermoser, D. Meier, and M. Trassin, The evolution of multiferroics, Nat. Rev. Mater. **1**, 16046 (2016).

[5] A. P. Pyatakov, Magnetoelectricity goes local: From bulk multiferroic crystals to ferroelectricity localized on magnetic topological textures, Physica B (Amsterdam, Neth.) **542**, 59 (2018).

[6] C. Beekman, W. Siemons, M. Chi, N. Balke, J. Y. Howe, T. Z. Ward, P. Maksymovych, J. D. Budai, J. Z. Tischler, R. Xu, W. Liu, and H. M. Christen, Ferroelectric self-poling, switching, and monoclinic domain configuration in $BiFeO_3$ thin films, Adv. Funct. Mater. **26**, 5166 (2016).

[7] R. K. Vasudevan, W. Wu, J. R. Guest, A. P. Baddorf, A. N. Morozovska, E. A. Eliseev, N. Balke, V. Nagarajan, and P. Maksymovych, Domain wall conduction and polarization-mediated transport in ferroelectrics, Adv. Funct. Mater. **23**, 2592 (2013).

[8] A. K.Yadav, C. T. Nelson, S. L. Hsu, Z. Hong, J. D. Clarkson, C. M. Schlepütz, A. R. Damodaran, P. Shafer, E. Arenholz, L. R. Dedon, D. Chen, A. Vishwanath, A. M. Minor, L. Q. Chen, J. F. Scott, L. W. Martin, and R. Ramesh, Observation of polar vortices in oxide superlattices, Nature (London) **530**, 198 (2016).

[9] E. Hassanpour, M. C. Weber, A. Bortis, Y. Tokunaga, Y. Taguchi, Y. Tokura, A. Cano, T. Lottermoser, and M. Fiebig, Interconversion of multiferroic domains and domain walls, arXiv:1908.06876.

[10] E. A. Eliseev, A. N. Morozovska, C. T. Nelson, and S. V. Kalinin, Intrinsic structural instabilities of domain walls driven by gradient couplings: Meandering anferrodistortive-ferroelectric domain walls in $BiFeO_3$, Phys. Rev. B **99**, 014112 (2019).

[11] M. J. Han, E. A. Eliseev, A. N. Morozovska, Y. L. Zhu, Y. L. Tang, Y. J. Wang, X. W. Guo, and X. L. Ma, Mapping gradient-driven morphological phase transition at the conductive domain walls of strained multiferroic films, Phys. Rev. B **100**, 104109 (2019).

[12] P. Sharma, P. Schoenherr, and J. Seidel, Functional ferroic domain walls for nanoelectronics, Materials **12**, 2927 (2019).

[13] S. Kawachi, S. Miyahara, T. Ito, A. Miyake, N. Furukawa, J. Yamaura, and M. Tokunaga, Direct coupling of ferromagnetic moment and ferroelectric polarization in $BiFeO_3$, Phys. Rev. B **100**, 140412(R) (2019).

[14] C. Tzschaschel, T. Satoh, and M. Fiebig, Tracking the ultrafast motion of an antiferromagnetic order parameter, Nat. Commun. **10**, 3995 (2019).

[15] A. Belianinov, Q. He, A. Dziaugys, P. Maksymovych, E. Eliseev, A. Borisevich, A. Morozovska, J. Banys, Y. Vysochanskii, and S. V. Kalinin, CuInPS room temperature layered ferroelectric, Nano Lett. **15**, 3808 (2015).

[16] M. A. Susner, M. Chyasnavichyus, M. A. McGuire, P. Ganesh, and P. Maksymovych, Metal thio- and selenophosphates as multifunctional van der Waals layered materials, Adv. Mater. **29**, 1602852 (2017).

[17] M. Wu and P. Jena, The rise of two-dimensional van der Waals ferroelectrics, Wiley Interdiscip. Rev.: Comput. Mol. Sci. **8**, e1365 (2018).

[18] F. Liu, L. You, K. L. Seyler, X. Li, P. Yu, J. Lin, X. Wang, J. Zhou, H. Wang, H. He, S. T. Pantelides, W. Zhou, P. Sharma, X. Xu, P. M. Ajayan, J. Wang, and Z. Liu, Room-temperature ferroelectricity in $CuInP_2S_6$ ultrathin flakes, Nat. Commun. **7**, 12357 (2016).

[19] X. Bourdon, V. Maisonneuve, V. B. Cajipe, C. Payen, and J. E. Fischer, Copper sublattice ordering in layered $CuMP_2Se_6$ (M = In, Cr), J. Alloys Compd. **283**, 122 (1999).

[20] Y.M. Vysochanskii, A. A. Molnar, M. I. Gurzan, V. B. Cajipe, and X. Bourdon, Dielectric measurement study of lamellar $CuInP_2Se_6$: Successive transitions towards a ferroelectric state via an incommensurate phase? Solid State Commun. **115**, 13 (2000).

[21] V. Liubachko, V. Shvalya, A. Oleaga, A. Salazar, A. Kohutych, A. Pogodin, and Y. M. Vysochanskii, Anisotropic thermal properties and ferroelectric phase transitions in layered $CuInP_2S_6$ and $CuInP_2Se_6$ crystals, J. Phys. Chem. Solids **111**, 324 (2017).

[22] J. A. Brehm, S. M. Neumayer, L. Tao, A. O'Hara, M. Chyasnavichus, M. A. Susner, M. A. McGuire, S. V. Kalinin,

S. Jesse, P. Ganesh, S. T. Pantelides, P. Maksymovych, and N. Balke, Tunable quadruple-well ferroelectric van der Waals crystals, Nat. Mater. **19**, 43 (2020).

[23] W. Song, R. Fei, and L. Yang, Off-plane polarization ordering in metal chalcogen diphosphates from bulk to monolayer, Phys. Rev. B **96**, 235420 (2017).

[24] Y. M. Vysochanskii, L. Beley, S. Perechinskii, M. Gurzan, O. Molnar, O. Mykajlo, V. Tovt, and V. Stephanovich, Phase transitions and disordering effects in $CuInP_2S(Se)_6$ layered ferrielectrics, Ferroelectrics **298**, 361 (2004).

[25] J. Macutkevic, J. Banys, R. Grigalaitis, and Yu. M. Vyschanskii, Asymmetric phase diagram of $CuInP_2(S_xSe_{1-x})_6$ crystals, Phys. Rev. B **78**, 064101 (2008).

[26] M. M. Maior, L. M. Belej, M. I. Gurzan, and Y. M. Vysochanskii, Peculiarities of the dipole ordering in $CuInP_2(Se_xS_{1-x})_6$ layered ferroelectrics, Ferroelectrics **349**, 71 (2007).

[27] Y. M. Vysochanskii, A. A. Molnar, M. I. Gurzan, and V. B. Cajipe, Phase transitions in $CuInP_2(Se_xS_{1-x})_6$ layered crystals, Ferroelectrics **257**, 147 (2001).

[28] L. M. Beley, O. A. Mykajlo, V. O. Stephanovych, I. P. Studenjak, M. I. Gurzan, and Y. M. Vysochanskii, Dipole glassy state evidence for $CuInP_2(Se, S)_6$ ferrielectric mixed crystals from Raman scattering and optical absorption data, Ukr., J. Phys. Opt. **8**, 14 (2007).

[29] M. M. Maior, S. F. Motrja, M. I. Gurzan, I. P. Pritz, and Yu. M. Vysochanskii, Dipole glassy state in layered mixed crystals of $Cu(In, Cr)P_2(S, Se)_6$ system, Ferroelectrics **376**, 9 (2008).

[30] S. M. Neumayer, E. A. Eliseev, M. A. Susner, B. J. Rodriguez, S. Jesse, S. V. Kalinin, M. A. McGuire, A. N. Morozovska, P. Maksymovych, and N. Balke, Giant negative electrostriction and dielectric tunability in a van der Waals layered ferroelectric, Phys. Rev. Materials **3**, 024401 (2019).

[31] A. Dziaugys, K. Kelley, J. A. Brehm, L. Tao, A. Puretzky, T. Feng, A. O'Hara, S. Neumayer, M. Chyasnavichyus, E. A. Eliseev, J. Banys, Y. Vysochanskii, F. Ye, B. C. Chakoumakos, M. A. Susner, M. A. McGuire, S. V. Kalinin, P. Ganesh, N. Balke, S. T. Pantelides, A. N. Morozovska, and P. Maksymovych, Piezoelectric domain walls in van der Waals antiferroelectric $CuInP_2Se_6$, Nat. Commun. **11**, 3623 (2020).

[32] A. N. Morozovska, E. A. Eliseev, D. Chen, C. T. Nelson, and S. V. Kalinin, Building free energy functional from atomically-resolved imaging: Atomic scale phenomena in la-doped $BiFeO_3$, Phys. Rev. B **99**, 195440 (2019).

[33] A. N. Morozovska, E. A. Eliseev, D. Chen, V. Shvetz, C. T. Nelson, and S. V. Kalinin, Melting of spatially modulated phases in la-doped $BiFeO_3$ at surfaces and surface-domain wall junctions, Phys. Rev. B **102**, 075426 (2020).

[34] I. Dzyaloshinsky, A thermodynamic theory of "weak" ferromagnetism of antiferromagnetics, J. Phys. Chem. Solids **4**, 241 (1958).

[35] E. A. Eliseev, Y. M. Fomichov, S. V. Kalinin, Y. M. Vysochanskii, P. Maksymovich, and A. N. Morozovska, Labyrinthine domains in ferroelectric nanoparticles: Manifestation of a gradient-induced morphological phase transition, Phys. Rev. B **98**, 054101 (2018).

[36] E. A. Eliseev and A. N. Morozovska, General approach for the description of size effects in ferroelectric nanosystems, J. Mater. Sci. **44**, 5149 (2009).

[37] O. D. Rodriguez Salmon and J. R. Tapia, Multicriticality in the blume-capel model under a continuous-field probability distribution, J. Phys. A: Math. Theor. **43**, 125003 (2010).

[38] See Supplemental Material http://link.aps.org/supplemental/10.1103/PhysRevB.102.174108 for calculation details.

[39] R. K. Behera, C.-W. Lee, D. Lee, A. N. Morozovska, S. B. Sinnott, A. Asthagiri, V. Gopalan, and S. R. Phillpot, Structure and energetics of 180° domain walls in $PbTiO_3$ by density functional theory, J. Phys.: Condens. Matter **23**, 175902 (2011).

[40] I. I. Ivanchyk, To macroscopic theory of ferroelectrics, Solid State Phys. **3**, 3731 (1961) (in Russian).

[41] A. N. Morozovska, E. A. Eliseev, Y. M. Fomichov, and S. V. Kalinin, Mesoscopic structure of mixed type domain walls in multiaxial ferroelectrics, Phys. Rev. Mater. **4**, 114410 (2020).

[42] http://creativecommons.org/licenses/by/4.0.

[43] http://creativecommons.org/licenses/by/4.0.